Investigation of flow regimes in arc plasma – gas interactions using a two-temperature arc in crossflow model

V G Bhigamudre[1] **and J P Trelles**[1, a)]

[1, a)] Department of Mechanical Engineering, University of Massachusetts Lowell,
One University Ave, Lowell, MA 01854, USA
E-mail: Juan_Trelles@uml.edu

Abstract. The perpendicular impingement of a gas stream on an electric arc, a configuration known as the arc in crossflow, is of primary relevance in the study of plasma-gas interactions, as well as in industrial applications such as circuit breakers and wire-arc spraying. The flow dynamics in the arc in crossflow are the result of coupled fluid-thermal-electromagnetic phenomena accompanied by large property gradients, which can produce significant deviations from Local Thermodynamic Equilibrium (LTE) among electrons and gas species. These characteristics can lead to the establishment of distinct flow regimes depending on the relative values of the controlling parameters of the system, such as inflow velocity, arc current, and inter-electrode spacing. A two-temperature non-LTE (NLTE) model is used to investigate the arc dynamics and the establishment of flow regimes in the arc in crossflow. The plasma flow model is implemented within a nonlinear Variational Multiscale (VMS) numerical discretization approach that is less dissipative, and hence better suited to capture unstable behavior, than traditional VMS methods commonly used in computational fluid dynamics simulations. The Reynolds and the Enthalpy dimensionless numbers, characterizing the relative flow strength and arc strength, respectively, are chosen as the controlling parameters of the system. Simulation results reveal the onset of dynamic behavior and the establishment of steady, periodic, quasi-periodic, and chaotic or potentially turbulent, regimes, as identified by distinct spatiotemporal fluctuations. The computational results reveal the role of increasing the relative arc strength on enhancing flow stability by delaying the growth of fluctuating and unstable flow behavior.

Keywords: Plasma stability, plasma-gas interaction, atmospheric pressure low-temperature plasma, thermodynamic nonequilibrium.

1. Introduction

1.1. The arc in crossflow

The arc in crossflow is a plasma configuration commonly encountered in industrial applications such as wire arc spraying and low-voltage circuit breakers, which involves the perpendicular impingement of a stream of gas onto an electric arc. The gas flow impingement causes the arc to bend and elongate downstream. The effects of the arc – gas flow interaction affect, for example, wire-arc spraying in terms of *process parameters*, such as particle dispersion [1, 2], droplet formation [3], particle trajectories [2, 4], atomization [1], and oxidation due to gas entrainment [5]; as well as *electrode parameters*, such as electrode erosion [6, 7], splitter erosion [8, 9], and asymmetric melting [10]. These phenomena may seem inter-dependent on each other (e.g., asymmetric melting can cause higher electrode erosion). Nevertheless, they are intrinsically the result of the strong plasma – gas flow interaction. This interaction is characterized by highly-coupled and complex physical phenomena such as imbalance between electromagnetic (Lorentz) and fluid dynamic drag forces, large temperature and density gradients, and marked deviations from Local Thermodynamic Equilibrium (LTE) between electrons and heavy-species (atoms, ions, molecules) [11]. In addition, the plasma – gas flow interaction can lead to the dynamic behavior of the arc, manifested by significant temperature and voltage fluctuations [12-14], which can markedly influence process characteristics.

The present work addresses the characterization of the intrinsic dynamics and the establishment of associated flow regimes in the arc in crossflow. These flow regimes depend on the relative values of the controlling parameters of the system, such as inflow velocity, arc current, and inter-electrode spacing. The present study adopts the Reynolds number, which characterizes the ratio of inertial to viscous forces, and the Enthalpy number, which characterizes the ratio of gas flow energy to electrical energy, as the main controlling parameters of the system. These controlling parameters are used to evaluate *qualitative* characteristics (i.e. the establishment of regimes such as steady, periodic, quasi-

periodic, as indicated by spatiotemporal property fluctuations), as well as *quantitative* characteristics (i.e., magnitude and frequency of fluctuations) of the arc in crossflow. The unraveling of these intrinsic flow characteristics elucidates fundamental aspects of plasma – gas interactions, and provides understanding that can aid in equipment and process design in arc in crossflow-based applications.

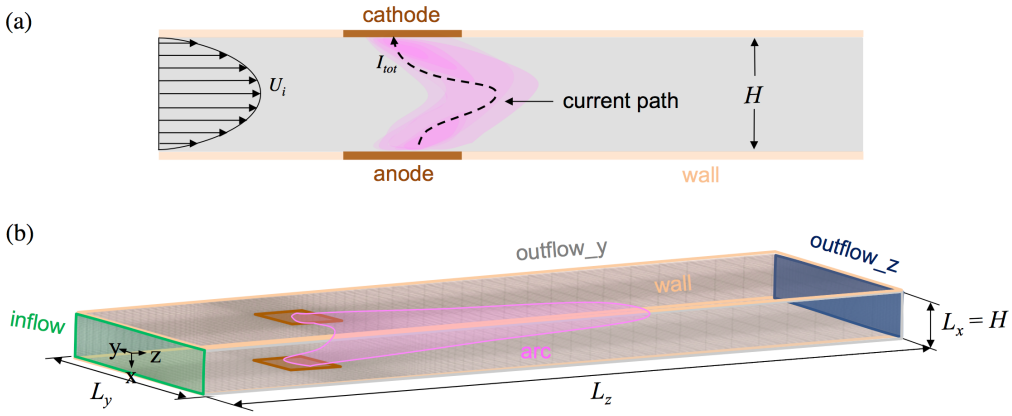

Figure 1. The arc in crossflow: (a) cross sectional view showing a bent arc of total current I_{tot} due to an impinging flow stream characterized by an inlet velocity U_i in between wall-embedded electrodes spaced a distance H; and (b) three-dimensional view of the computational domain and its boundaries.

A schematic representation of the arc in crossflow model is presented in figure 1. The main parameters of the system are: working gas type, total current I_{tot}, inlet gas velocity U_i, and electrode gap H. The model is applied to an arc discharge in pure argon. As indicated in figure 1(a), the interaction of plasma – gas flow interaction causes the bending of the arc, which consequently leads to large property gradients and coupled thermal-fluid-electromagnetic phenomena [15, 16]. Figure 1(b) presents the computational domain for the solution of the model, including the domain's geometric parameters and boundaries. The present study builds on the prior computational characterization of the arc in crossflow presented in references [11, 17].

1.2. Computational study of plasma dynamics

Plasma flow dynamics have been studied more thoroughly, compared to the arc in crossflow, in configurations such as plasma torches and pin-to-plate set-ups due to their direct relevance to

industrial applications (e.g. plasma spraying and welding, respectively) [2, 18-24]. The dynamics involved in these configurations are significantly involved, with several inter-related physical phenomena, such as continuous change in the arc length [25], azimuthal rotation of the arc [26], arc root movement [10], etc. Such dynamic interplay leads, for example, to different arc modes in non-transferred arc plasma torches [18, 27]. In contrast to the arc systems above, the arc in crossflow is significantly simpler, yet it acts as a canonical configuration for the study of plasma – gas flow interactions [28, 29], offering fundamental understanding of arc plasma dynamics.

Computational investigations offer distinct advantages compared to experimental diagnostics, such as concurrent estimation of distributed solution (pressure, temperature, velocity, electric potential, etc.) and derived (magnetic field, Lorentz force, current density, etc.) fields. Computational studies of plasma dynamics necessarily require utilizing time-dependent models (to resolve temporal fluctuations) in three-dimensional (3D) spatial domains (to track the spatial evolution of fluctuations), which make them computationally expensive. The computational expense of the study of plasma – gas flow interactions is exacerbated considering that the associated large temperature, density, and property gradients along with complex multi-physical phenomena (such as fluid dynamics, heat transfer, chemical kinetics and electromagnetics) ultimately leading to turbulence [13] – the outmost computationally demanding fluid flow phenomena to simulate. Diverse research works have addressed the computational cost associate to the study of plasma flow dynamics at the expense of using simplified models, such as assuming the plasma to be in a LTE state [25, 30]. However, the LTE assumption is valid only in the plasma core, and significant deviations are expected in strong plasma – gas interactions, thermal boundary layers [2, 18], etc. In this regard, Non-LTE (NLTE) plasma flow models [12, 31] can be better suited than LTE models [32, 33] for the study of plasma – gas flow interactions. Moreover, the need to resolve dynamic behavior and instabilities imposes additional requirements in terms of the numerical resolution of the computational model, such as the use of fine temporal and spatial discretizations (computational grids or meshes, and time steps) and low-dissipation schemes [34].

1.3. Outline

The article is organized as follows: Section 2 presents the mathematical model, the numerical approach, and the computational model setup. The controlling parameters of the system are presented in Section 3. Section 4 describes the approach used to identify and characterize the arc dynamics, the role of the numerical approach on the obtained solutions, and the effect of controlling parameters on the arc dynamics. Results of the identification of arc in crossflow regimes and their characteristics are presented in Section 5. Summarizing and concluding remarks are presented in Section 6.

2. Computational Model

2.1. Mathematical model

The plasma is considered as an optically thin, quasi-neutral, non-magnetized, compressible, reactive, and electromagnetic fluid in chemical equilibrium and thermal nonequilibrium (two-temperature NLTE). Ion diffusion, Hall currents, and electrode sheaths are neglected. The mathematical model is constituted by the equations of conservation of total mass, mass-average momentum, thermal energy of heavy-species, and thermal energy of electrons, and the equations for electric charge conservation and of magnetic induction. These equations are listed in table 1 in transient-advective-diffusive-reactive (TADR) form.

In table 1, $\partial_t = \partial / \partial t$ is the partial time derivative, ∇ and $\nabla\cdot$ are the gradient and divergence operators, respectively; ρ is mass density, p pressure, $\mathbf{u}$ mass-averaged velocity, μ dynamic viscosity, $^{\mathsf{T}}$ the transpose operator, and $\boldsymbol{\delta}$ the Kronecker delta tensor; $\mathbf{J}_q$ is the electric current density and $\mathbf{B}$ is the self-induced magnetic field; h_h and h_e are the enthalpies, and T_h and T_e are the temperatures, of the heavy-species and electrons, respectively; κ_{hr} is the heavy-species translational-reactive thermal conductivity, κ_e is the translational electron thermal conductivity, $D_t p$ is the pressure work, where $D_t \equiv \partial_t + \mathbf{u}\cdot\nabla$ represents the total derivative, and $p = p_h + p_e$ represents the total pressure, with p_h and p_e the heavy-species and electron pressure, respectively; K_{eh} is the energy exchange coefficient between heavy-species and electrons, $\boldsymbol{\tau}$ is the stress tensor for a Newtonian fluid, ε_r is effective net

radiative emission coefficient; **E** is the *real* electric field, k_B Boltzmann constant, e the elementary electric charge, ϕ_p is the *effective* electric potential, and **A** is the magnetic vector potential.

The set of TADR equations is treated in monolithic form as a single system given by:

$$\mathcal{R}(\mathbf{Y}) = \underbrace{\mathbf{A_0}\partial_t \mathbf{Y}}_{\text{transient}} + \underbrace{(\mathbf{A}_i\partial_i)\mathbf{Y}}_{\text{advective}} - \underbrace{\partial_i(\mathbf{K}_{ij}\partial_j \mathbf{Y})}_{\text{diffusive}} - \underbrace{(\mathbf{S_1 Y} + \mathbf{S_0})}_{\text{reactive}} = \mathbf{0}, \tag{1}$$

where $\mathcal{R}$ is the residual vector, **Y** the vector of unknowns, $\mathbf{A_0}$, $\mathbf{A}_i$, $\mathbf{K}_{ij}$, $\mathbf{S_1}$, $\mathbf{S_0}$ are coefficient matrices that describe the different transport processes, i and j are spatial indices, and Einstein's convention of repeated indexes is used. Equation (1) is solved for the set of primate variables:

$$\mathbf{Y} = [p \;\; \mathbf{u} \;\; T_h \;\; T_e \;\; \phi_p \;\; \mathbf{A}]. \tag{2}$$

The model is complemented by the definition of thermodynamic (h_h, h_e etc.) and transport (μ, κ_e, etc.) material properties (data used from [35] and references within), as well as by constitutive relations ($\mathbf{J}_q = \sigma(\mathbf{E} + \mathbf{u} \times \mathbf{B})$, $\mathbf{B} = \nabla \times \mathbf{A}$, etc.). A detailed description of the model is presented in [11, 35].

Table 1. Evolution equations for the two-temperature NLTE plasma flow model. For all equations: Transient + Advective – Diffusive − Reactive = 0.

Equation	**Transient**	**Advective**	**Diffusive**	**Reactive**
Mass conservation	$\partial_t \rho$	$\mathbf{u}\cdot\nabla\rho + \rho\nabla\cdot\mathbf{u}$	0	0
Momentum conservation	$\rho\partial_t \mathbf{u}$	$\rho\mathbf{u}\cdot\nabla\mathbf{u} + \nabla p$	$\nabla\cdot\mu(\nabla\mathbf{u} + \nabla\mathbf{u}^{\mathsf{T}}) - \nabla\cdot(\frac{2}{3}\mu(\nabla\cdot\mathbf{u})\boldsymbol{\delta})$	$\mathbf{J}_q \times \mathbf{B}$
Thermal energy heavy-species	$\rho\partial_t h_h$	$\rho\mathbf{u}\cdot\nabla h_h$	$\nabla\cdot(\kappa_{hr}\nabla T_h)$	$D_t p_h + K_{eh}(T_e - T_h) - \boldsymbol{\tau} : \nabla\mathbf{u}$
Thermal energy electrons	$\rho\partial_t h_e$	$\rho\mathbf{u}\cdot\nabla h_e$	$\nabla\cdot(\kappa_e\nabla T_e)$	$D_t p_e - K_{eh}(T_e - T_h) - 4\pi\varepsilon_r + \mathbf{J}_q\cdot(\mathbf{E} + \mathbf{u}\times\mathbf{B}) + \frac{5k_B}{2e}\mathbf{J}_q\cdot\nabla T_e$
Charge conservation	0	0	$\nabla\cdot(\sigma\nabla\phi_p) - \nabla\cdot(\sigma\mathbf{u}\times(\nabla\times\mathbf{A}))$	0
Magnetic induction	$\mu_0\sigma\partial_t\mathbf{A}$	$\mu_0\sigma\nabla\phi_p - \mu_0\sigma\mathbf{u}\times(\nabla\times\mathbf{A})$	$\nabla^2\mathbf{A}$	$\mathbf{0}$

The evaluation of the above NLTE model against a LTE model [32] and experimental results has been presented in [11]. The investigation in [11] showed that results from the two-temperature model present better agreement with experimental observations than the LTE model, while providing quantification of the deviation between heavy-species and electron temperatures. Moreover, the use of the LTE assumption generally leads to over prediction of the arc voltage drop across the arc. For example, in twin torch systems [36] and plasma torches [31] the arc voltage drop obtained with an LTE model is significantly higher than that using an NLTE one. Therefore, the present work focuses on the exploration and identification of flow regimes using a NLTE model only.

2.2. Numerical model

Computational thermal plasma flow simulations inherently involve large and nonlinear variations in solution fields and material properties, which makes the associated models numerically stiff and hence require the use of robust discretization and numerical techniques for their solution. Due to their inherent advantages, Finite Element Methods (FEMs) are widely used in diverse fields, including plasma flow modeling. Among FEMs, stabilized and particularly, Variational Multiscale (VMS) methods, have demonstrated to be particularly effective dealing with highly multiscale phenomena [37]. VMS methods have been used to solve scalar transport, radiation transport, incompressible, compressible, reactive, magnetohydrodynamics, and turbulent flow problems [35], as well as nonequilibrium plasma flows [11, 12, 27, 31, 38-41].

Recently, ModirKhazeni and Trelles [42] have presented a VMS formulation that provides a better description of the intricate nonlinear coupling between the large-scales and the small-scales of the solution fields termed non-linear Variational Multiscale (VMS_n). (The large-scales are those actually captured by the discretization and the small-scales are unresolved sub-grid features.) VMS_n has demonstrated to be effective for the unified simulation of incompressible and compressible laminar and turbulent flow problems, as well as the flow from a non-transferred arc plasma torch [42], providing greater accuracy than a VMS approach. The greater accuracy of the VMS_n method has prompted its adoption in the present research of the arc in crossflow.

VMS methods start with a Galerkin formulation of the problem given by Eq. (1), i.e.,

$$\int_{\Omega} \mathbf{W} \cdot \mathcal{R}(\mathbf{Y}) d\Omega = (\mathbf{W}, \mathcal{R}(\mathbf{Y}))_{\Omega} = (\mathbf{W}, \mathcal{L}\mathbf{Y} - \mathbf{S_0})_{\Omega} = \mathbf{0}, \tag{3}$$

where Ω is the spatial domain, $\mathbf{W}$ the weight function, and $\mathcal{L}$ is the transport operator defined from $\mathcal{R}(\mathbf{Y}) = \mathcal{L}\mathbf{Y} - \mathbf{S_0}$. Then, $\mathbf{Y}$ and $\mathbf{W}$ are decomposed into large- and small-scales, i.e. $\mathbf{Y} = \bar{\mathbf{Y}} + \mathbf{Y}'$ and $\mathbf{W} = \bar{\mathbf{W}} + \mathbf{W}'$. The use of traditional VMS methods assumes $\mathcal{L} = \mathcal{L}(\mathbf{Y}) = \mathcal{L}(\bar{\mathbf{Y}} + \mathbf{Y}') \approx \mathcal{L}(\bar{\mathbf{Y}})$; this is, the effect of the small-scales in the transport operator is neglected. The small-scales are subsequently calculated by an algebraic approximation as $\mathbf{Y}' \approx -\boldsymbol{\tau}\mathcal{R}(\bar{\mathbf{Y}})$, where $\boldsymbol{\tau}$ is the so-called *intrinsic time scales matrix* such that $\boldsymbol{\tau} \approx \mathcal{L}^{-1}$. Using this approximation, equation (3) can be treated as a function of large-scale *alone*. The VMS method's implementation and validation for the simulation of nonequilibrium thermal plasma flows, including a previous study of the arc in crossflow, are shown in [35].

The approximation $\mathcal{L}(\mathbf{Y}) \approx \mathcal{L}(\bar{\mathbf{Y}})$ in traditional VMS methods is generally valid for many flow problems, but it is generally inadequate for problems in which the small-scales play a major role, such as in transitional and turbulent flows. The VMS$_n$ method addresses the nonlinearity of the transport operator upfront, i.e. $\mathcal{L} = \mathcal{L}(\bar{\mathbf{Y}} + \mathbf{Y}')$. This result in two equations to be solved concurrently, one for large- and one for small- scales each, i.e.:

$$\underbrace{(\bar{\mathbf{W}}, \mathcal{L}\bar{\mathbf{Y}} - \bar{\mathbf{S}}_0)_{\Omega} + (\mathcal{L}^{*}\bar{\mathbf{W}}, \mathbf{Y}')_{\Omega} = \mathbf{0}}_{\text{large-scales}} \quad \text{and} \quad \underbrace{(\mathbf{W}', \mathcal{L}\bar{\mathbf{Y}} - \bar{\mathbf{S}}_0)_{\Omega} + (\mathcal{L}^{*}\mathbf{W}', \mathbf{Y}')_{\Omega} = \mathbf{0}}_{\text{small-scales}}, \tag{4}$$

where * denotes the adjoint operator. The intrinsic time scale matrix is also a nonlinear function, i.e. $\boldsymbol{\tau} = \boldsymbol{\tau}(\bar{\mathbf{Y}} + \mathbf{Y}')$. The nonlinearity of $\mathcal{L}$ and $\boldsymbol{\tau}$ requires the use of a nonlinear solution approach for the solution of Eq. (4). This is accomplished using a fixed-point (Picard) iteration given by:

$$\mathcal{L}^{n+1} = \mathcal{L}(\bar{\mathbf{Y}} + \mathbf{Y}'^{n}), \boldsymbol{\tau}^{n+1} = \boldsymbol{\tau}(\bar{\mathbf{Y}} + \mathbf{Y}'^{n}), \mathbf{Y}'^{n+1} = -\boldsymbol{\tau}^{n+1}(\mathcal{L}^{n+1}\bar{\mathbf{Y}} - \bar{\mathbf{S}}_0), \tag{5}$$

where n indicates the iteration counter and the iteration starts with $\mathbf{Y}'^{0} = \mathbf{0}$. It is to be noted that if n = 0, the VMS$_n$ results in the VMS method; i.e., $\mathcal{L} = \mathcal{L}(\bar{\mathbf{Y}})$, $\boldsymbol{\tau} = \boldsymbol{\tau}(\bar{\mathbf{Y}})$, and $\mathbf{Y}' \approx -\boldsymbol{\tau}(\mathcal{L}\bar{\mathbf{Y}} - \bar{\mathbf{S}}_0)$.

The final VMS$_n$ formulation is given by concurrent iterative solution of the equations [12, 35]:

$$\bar{\mathbf{R}}(\mathbf{Y}_h;\mathbf{Y}') = \underbrace{(\mathbf{N},(\mathbf{A}_0\partial_t + \mathbf{A}_i\partial_i - \mathbf{S}_1)\mathbf{Y}_h - \mathbf{S}_0)_\Omega + (\partial_i\mathbf{N},\mathbf{K}_{ij}\partial_j\mathbf{Y}_h)_\Omega - (\mathbf{N},\mathbf{K}_{ij}\partial_j\mathbf{Y}_h)_\Gamma}_{\text{large-scales}}$$
$$+ \underbrace{((\mathbf{A}_0^\mathsf{T}\partial_t + \mathbf{A}_i^\mathsf{T}\partial_i + \partial_i(\mathbf{K}_{ij}^\mathsf{T}\partial_j) + \mathbf{S}_1^\mathsf{T})\mathbf{N},\mathbf{Y}')_{\Omega'}}_{\text{small-scales}} + \underbrace{(\partial_i\mathbf{N},\mathbf{K}_{ij}^{DC}\partial_j\mathbf{Y}_h)_{\Omega'}}_{\text{discontinuity capturing}} = \mathbf{0}, \text{ and} \tag{6}$$

$$\mathbf{R}'(\mathbf{Y}';\mathbf{Y}_h) = \mathbf{Y}' + \boldsymbol{\tau}(\mathcal{L}\mathbf{Y}_h - \mathbf{S}_0) = \mathbf{0}, \tag{7}$$

where **N** is the basis function (i.e. FEM interpolation function); and the notation $f(a;b)$ indicates that a is an argument of the equation and b a parameter. In Eq. (6) a *discontinuity-capturing* operator is added to minimize the occurrence of spurious oscillations near unresolved high-gradient regions as well as to increase the robustness of the solution approach. Details about the numerical solution approach are found in [35].

VMS methods, by resolving the large-scales and modeling the small-scales of the solution, constitute coarse-grained simulation approaches, equivalent to Large Eddy Simulation (LES) methods for the simulation of turbulent flows [54-56]. Yet, in contrast to traditional LES methods, which rely on Smagorinsky-like models to model small-scale interactions, VMS methods rely on a local approximation of small-scales problem (i.e. $\mathbf{Y}' \approx -\boldsymbol{\tau}(\mathcal{L}\bar{\mathbf{Y}} - \bar{\mathbf{S}}_0)$). This characteristic makes VMS approaches particularly appealing for the computational modeling of highly nonlinear flow problems, such as plasma flows.

2.3. Geometrical configuration and boundary conditions

The geometrical dimensions of the computational domain for the arc in crossflow in figure 1 are: L_x x L_y x L_z = 2 mm x 10.1 mm x 37 mm. The electrodes are squares of size $d_y = d_z$ = 3 mm. The inter-electrode distance ($L_x = H$) is the most important dimension for the arc in crossflow, as it strongly influences the characteristics of the arc column. The dimensions L_y and L_z can be chosen freely as long as the plasma remains well within the computational domain (L_y) and the extent of the domain does not alter the arc behavior (L_z). The computational domain is discretized using a semi-structured tri-linear hexahedral elements grid of ~ 250000 nodes. This is in contrast to the simulations reported in [11], which used a significantly coarser grid of ~ 85000 nodes. Additionally, the current work used a model discretization based on the VMS$_n$ method described in section 2.2; which is also in contrast to the

simulations reported in [11] based on a classical VMS method. The higher numerical resolution and improved numerical discretization approach were required in the present work in order to resolve the onset of instabilities and to attain convergent solutions for a wider range of controlling parameters than those used in [11]. A comparison between results obtained with the VMS and VMS$_n$ methods, for the same spatial discretization, is presented in section 4.3.

Table 2 lists the set of boundary conditions used to describe the problem. In Table 2, n represents the outer normal direction to the corresponding boundary. The outflow_z boundary is set to be at atmospheric pressure, i.e. $p = p_\infty = 1.01325 \cdot 10^5$ Pa, while at all other boundaries a zero-pressure gradient normal to the surface is imposed. For the inflow boundary, the velocity profile is imposed such that it is maximum at the center and minimum at the edges, i.e. $\mathbf{u_i} = [u_{ix}\ u_{iy}\ u_{iz}]^\mathsf{T} = [\ 0\ 0\ U_i\ ]$, where $U_i(x) = U_{imax}(1 - (x/H)^2)$. The no-slip condition (i.e. $\mathbf{u} = \mathbf{0}$) is imposed over electrode surfaces and to the solid surfaces surrounding them (i.e. anode, cathode, and walls).

Table 2. Set of boundary conditions for the arc in crossflow.

Boundary	p	$\mathbf{u}$	T_h	T_e	ϕ_p	$\mathbf{A}$
inflow	$\partial_n p = 0$	$\mathbf{u} = \mathbf{u_i}$	$T_h = T_0$	$T_e = T_0$	$\partial_n \phi_p = 0$	$\mathbf{A} = \mathbf{0}$
anode	$\partial_n p = 0$	$\mathbf{u} = \mathbf{0}$	$-k_h \partial_n T_h = h_w (T_h - T_w)$	$\partial_n T_e = 0$	$\phi_p = 0$	$\partial_n \mathbf{A} = \mathbf{0}$
cathode	$\partial_n p = 0$	$\mathbf{u} = \mathbf{0}$	$T_h = T_c$	$\partial_n T_e = 0$	$-\sigma \partial_n \phi_p = J_{qcath}$	$\partial_n \mathbf{A} = \mathbf{0}$
wall	$\partial_n p = 0$	$\mathbf{u} = \mathbf{0}$	$-k_h \partial_n T_h = h_w (T_h - T_w)$	$\partial_n T_e = 0$	$\partial_n \phi_p = 0$	$\partial_n \mathbf{A} = \mathbf{0}$
outflow_z	$p = p_\infty$	$\partial_n \mathbf{u} = \mathbf{0}$	$\partial_n T_h = 0$	$\partial_n T_e = 0$	$\partial_n \phi_p = 0$	$\partial_n \mathbf{A} = \mathbf{0}$
outflow_y	$\partial_n p = 0$	$\partial_n \mathbf{u} = \mathbf{0}$	$\partial_n T_h = 0$	$\partial_n T_e = 0$	$\partial_n \phi_p = 0$	$\partial_n \mathbf{A} = \mathbf{0}$

A heavy-species temperature $T_h = T_0 = 500$ K is imposed at the inlet. A parabolic heavy-species temperature distribution is specified on the cathode surface $T_c = T_{c0}(1-(y/y_{cath})^2 - ((z-z_{off})/z_{cath})^2)$, where the maximum cathode temperature $T_{c0} = 3000$ K (approximately equal to the melting point for Tungsten [28]) and the minimum value of T_c occurs along the cathode boundaries with a value close to the wall-cooling reference temperature $T_w = 1000$ K; y and z are the spatial coordinates, y_{cath} and z_{cath}

are the characteristic electrode lengths ($y_{cath} = z_{cath} = d_x/2 = d_y/2 = 1.5$ mm), and z_{off} is the offset distance from the origin to the center of the cathode. The anode and wall boundaries are described as experiencing forced water cooling over a metal surface with a convective heat transfer coefficient of [31, 35] $h_w = 2 \cdot 10^4$ $\mathrm{Wm^{-2}K^{-1}}$, and reference wall temperature $T_w = 500$ K. Such model is a rough approximation of the heat transfer from the plasma through the walls, yet an approximation extensively used in thermal plasma flow simulations [27]. A more adequate model involves including part of the solid wall within the computational domain, as done in [52,53]. Finally, the electron temperature, T_e is imposed with zero normal gradient condition over all the boundaries except at the inflow, where the inflow gas is assumed to be in LTE, i.e. $T_e = T_h = T_0$ [44].

The current density J_{qcath} profile follows a quasi-Gaussian distribution over the cathode boundary, i.e., $J_{qcath} = J_{qcath0} \exp(-(r/R_c)^{n_c})$, where $r = (x^2 + y^2)^{\frac{1}{2}}$ is the radial coordinate; n_c, R_c and J_{qcath0} are applied such that the total current $I_{tot} = \int J_{qcath}\, dS$, and S represents the area of the cathode surface.

3. Controlling parameters

The main parameters of the arc in crossflow are the total current I_{tot}, the inflow velocity U_{imax}, the inter-electrode spacing H, and the type of gas (figure 1(a)). The effects of the total current and the inflow velocity on the arc in crossflow have been studied experimentally [45], as well as computationally [32, 33]. A computational characterization of the arc in crossflow was presented in [11] using two non-dimensional numbers: the Reynolds number Re and the Enthalpy number Π_h. A similar approach is pursued in this study. The Reynolds number Re characterizes the ratio of the magnitudes of advective transport to diffusive transport. In contrast to [11], the definition of the Enthalpy number used in the present work Π_I characterizes the ratio of the magnitudes of electrical energy to thermal energy transport (i.e. $\Pi_I = \Pi_h^{-1}$). The Reynolds number can be understood as characterizing the *strength of the flow*, i.e. the stronger the flow, the larger the Re. Similarly, the Enthalpy number characterizes the *strength of the arc*, i.e. the stronger the arc, the larger the Π_I.

The Reynolds and the Enthalpy numbers for the present study are defined by:

$$Re = \frac{\rho_i U_{i\max} H}{\mu_i} \quad \text{and} \tag{8}$$

$$\Pi_I = \frac{I_{tot}^2}{\sigma_r h_r \rho_r U_{i\max} H^3}, \tag{9}$$

where the subscripts '*r*' denotes the property evaluated at a reference discharge temperature and '*i*' denotes values evaluated at the inlet conditions. In the present work, the reference temperature is set to 16.7 kK, which corresponds to a recommended representative temperature for an argon plasma [15].

4. Results and discussions

4.1. Solution fields

Representative three-dimensional (3D) steady-state solution fields are presented in figure 2 for two representative conditions: (*left column*) strong-flow – weak-arc, corresponding to Re = 8630 and Π_I = 85.4, and (*right column*) weak-flow – strong-arc, corresponding to Re = 3000 and Π_I = 800.

The resulting arc shape is the result of the imbalance between the electromagnetic force emerging due to the electromagnetic field distribution and the drag force caused by the gas flow. Experimental observations of emission intensity [28] are often used to characterize the arc shape. In that regards, the value of an effective excitation temperature, responsible of most optical emission, can be expected to lie in between the values of T_e and T_h. Therefore, the actual arc shape can be expected to be somewhat in between the distributions of the heavy-species temperature T_h (figure 2(a)) and the electron temperature distribution T_e (figure 2(b)). For the strong-flow – weak-arc configuration (figure 2, *left*), the arc bends more profoundly at the arc – gas interface, leading it to become bow-shaped; whereas for the weak-flow – strong-arc configuration (figure 2, *right*), the arc is lead to be cusp-shaped. The arc – gas interface is characterized by a marked increase in the degree of thermodynamic nonequilibrium, characterized by the electron-to-heavy-species temperature ratio $\theta = T_e/T_h$. The distribution of the thermodynamic nonequilibrium parameter θ and the effects of the controlling parameters on the arc shape in the arc in crossflow plasma were discussed in [11].

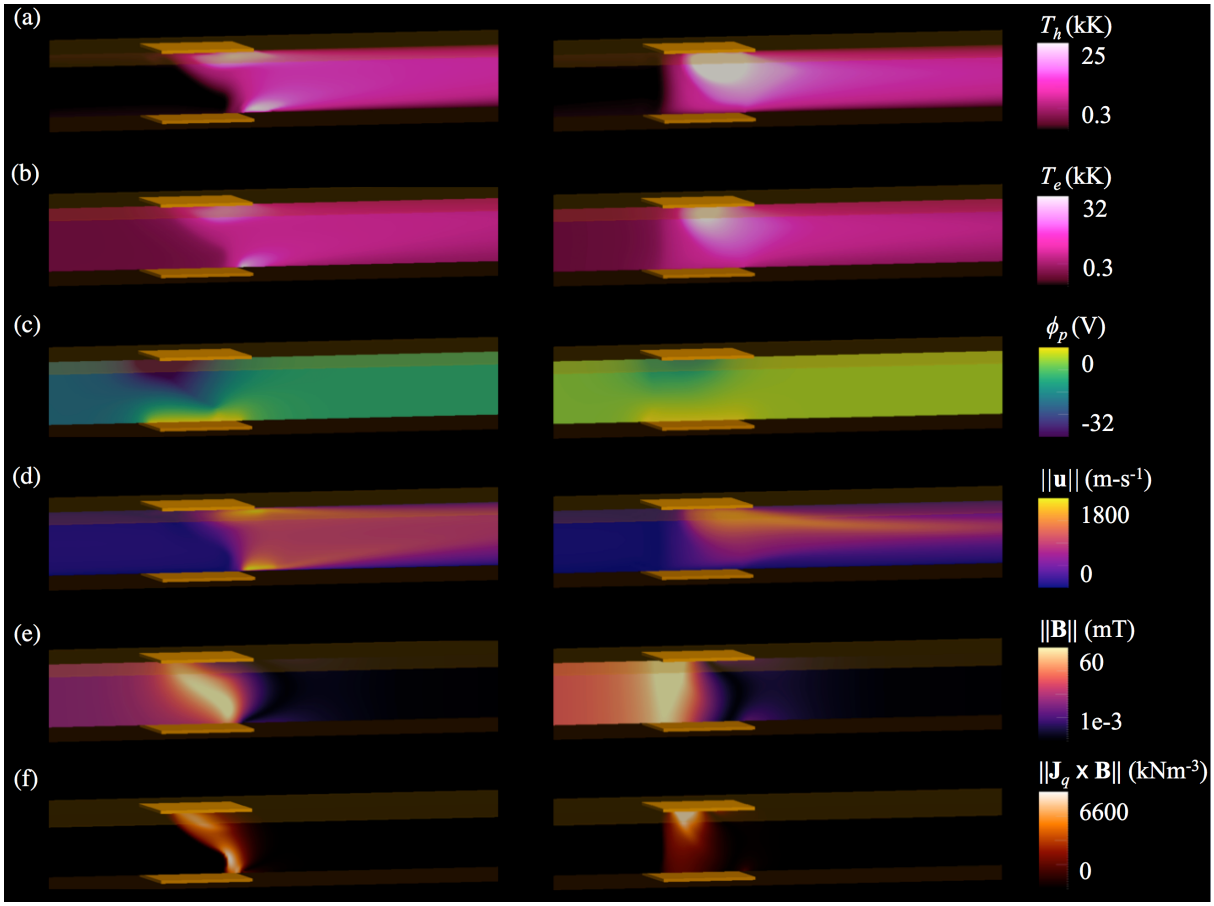

Figure 2. Representative steady-state solution fields for two representative conditions: (*left*) strong-flow – weak-arc (*Re* = 8630 and Π_I = 85.4) and (*right*) weak-flow – strong-arc (*Re* = 3000 and Π_I = 800): (a) heavy-species temperature, (b) electron temperature, (c) electric potential, (d) velocity magnitude, (e) self-induced magnetic field magnitude, and (f) Lorentz force magnitude.

The results in figure 2 show that the electric potential distribution is more diffusive for the weak-flow – strong-arc configuration, while the strong-flow – weak-arc configuration shows an abrupt change. The abrupt change of the electric potential occurs at the region where the arc bends due to strong drag force and is characterized with greater magnitude of the electric field leading to a dramatic directional change in the current path (for very high gas flow rates, the bending angle can be close to 180°). It is interesting to note that the electric potential distribution is a maximum at the electrode center for the weak-flow – strong-arc configuration, whereas the maximum shifts upstream with increasing the gas flow rate. This behavior may be the result of the strong influx of

electrons from the plasma core to the plasma – cathode – gas interface [29], which leads to a high degree of thermodynamic nonequilibrium.

To better capture the plasma cathode interaction, the grid size should be small enough to resolve the strong gradients of the solution fields (e.g., heavy-species temperature, velocity). Moreover, the plasma flow model should be complemented with sheath model to better describe charge transport phenomena near the electrodes. A limitation of the arc in crossflow model used in the present study is that the model cannot appropriately describe near-electrode phenomena (i.e. electrode sheaths). The coupling of NLTE-plasma flow – plasma-sheath model is an active area of research [27, 46, 47], which is beyond the aim of the present work.

The velocity magnitude $\|\mathbf{u}\|$ depends strongly on the imposed electric current and on the inflow gas velocity. The imposed current causes strong Joule heating and the gas inflow causes the cooling of the arc; their combined effect lead to a drastic increase in local velocity, as shown in figure 2(d). The velocity magnitude $\|\mathbf{u}\|$ distribution shows distinct characteristics in the electrode upstream and in the electrode downstream regions, i.e., the gradient of velocity magnitude is more intense downstream of the electrode than upstream. For high-power arcs (e.g., high current, $I_{tot} > 200$ A, and flow rates, $U_i >$ 100 m-s^{-1}), the gradient extends further downstream, causing the attachment to extend along the wall. The velocity magnitude in NLTE model simulations is significantly higher than those obtained in LTE simulations. For example, Kelkar and Heberlein reported maximum velocities of up to 1300 ms^{-1} using a LTE model [32]; whereas the NLTE model used here leads to maximum velocities of ~1560 ms^{-1} for a coarse grid (~85000 nodes) [11] and velocities of ~1800 ms^{-1} with the finer grid used in the present study. The large discrepancies appear to be the result to the larger heavy-species temperatures obtained with NLTE models compared to those from LTE ones [11, 31, 36], as well as the greater resolution of heavy-species temperature gradients, particularly near the cathode region. Higher heavy-species temperature T_h leads to lower mass density ρ, which induces larger velocities in order to maintain mass flow ($\rho\mathbf{u}$) continuity. The Mach number $Ma = \|\mathbf{u}\|/c = \|\mathbf{u}\|/(\partial p/\partial\rho)^{1/2}$, where c is the speed of sound, indicates that the inflow conditions lead to a largely sub-sonic flow

(i.e. $Ma_i << 1$). Despite the large acceleration of the flow in the arc core (maximum $||\mathbf{u}|| \sim 1800$ ms^{-1}), the local *Ma* remains less than one everywhere given that $c \sim 10^3$ to 10^4 ms^{-1} within the arc [35].

As seen in figure 2(e), the self-induced magnetic field increases at the arc – gas flow interface and reduces to a minimum in the plasma core. The magnitudes of the obtained magnetic fields are comparable to those reported in the computational simulation of circuit breakers, i.e. ~ 60 mT in the simulations here compared to ~ 45 mT reported in [9]. The Lorentz force distribution is similar to the magnetic field distribution; nevertheless, the former presents a relatively larger gradient near the electrodes, particularly near the cathode, due to the high values and constriction of current density. The magnitude of Lorentz force is in the order of 10^6 N-m^{-3}, which is significantly larger than the values of $\sim 10^4$ N-m^{-3} reported in the simulation of an inductively-coupled plasma (ICP) torch in [48] (torch diameter of 8 mm). The magnitude of the Lorentz force decreases drastically in the region near the mid-plane (mid inter-electrode region), as expected due to the weaker magnetic field and more diffuse distribution of current density.

4.2. Arc dynamics

There are significantly fewer investigations of the dynamics in the arc in crossflow compared to those found in other arc configurations, such as non-transferred plasma torches [10, 21, 22]. Non-transferred arc plasma torches experience complex plasma – gas interactions that often lead to the azimuthal rotation and continuously elongation of the arc; its subsequent extinguishment, and re-establishment at a different, near-cathode, location. In contrast, the arc in crossflow is a canonical configuration that involves perpendicular plasma – gas interaction leading to a relatively constant arc, a characteristic that makes this configuration ideal for the study of arc - gas glow interactions. Nevertheless, the obtained simulation results show that the arc tends to develop temporal fluctuations depending on the values of the controlling parameter *Re* and Π_I. These fluctuations are the result of: (*i*) the continuous competition between electromagnetic and flow drag forces, (*ii*) the occurrence of thermal nonequilibrium, and (*iii*) the large variation of plasma material properties.

The arc in crossflow simulations are run for an extent of time that is function of the intrinsic characteristic time $t_{char} = L_z/U_{imax}$. This intrinsic time can be understood as a characteristic transit time for a particle to navigate the whole axial extent of the domain. The dynamic characteristics of the flow are then represented as function of the dimensionless time t/t_{char}. To discern representative dynamic behavior of the flow, four representative spatial observation-points are defined, as indicated in figure 3. Figure 3(a) shows the placement of the observation-points: one near the cathode (Near-cathode) and three along the center of the channel (i.e. Upstream, Midstream, and Downstream). The Near-cathode location is 0.3 mm away from the center of the cathode (figure 3(b)). The Upstream observation-point is placed at the midpoint in between the electrodes (center of the channel); and the Midstream and the Downstream points are placed 10 and 20 mm, respectively, downstream from it along the channel's center axis. To make the observation-points data grid-independent (i.e. not function of the size of the discretization grid), as well as to make the results more consistent with experimental measurements (e.g. via probes), each observation-point consists of a cubic element of side 0.2 mm, as shown in figure 3(b). The reported data from a given observation point corresponds to the volume-average of the distribution of the corresponding data over the corresponding cube.

To identify the flow dynamics, fluctuation signals are extracted from the observation-points data. Representative fluctuation signals are presented in figure 3(c) for the heavy-species temperature T_h and for the conditions Re = 8630 and Π_I = 85.4, i.e. the strong-flow – weak-arc studied in figure 2 (*left*). The fluctuation signal is given by $\delta T_h = (T_h - \overline{T}_h)/\overline{T}_h$, where $\overline{T}_h$ is the time-averaged value at steady-state. As observed in figure 3(c), T_h in the Upstream point varies by over 15% with respect to its mean; whereas it at the Near-cathode, Midstream, and Downstream locations, it varies by less than 5%. The drastic change in δT_h along the electrode axis might indicate marked dynamics at the plasma-arc – gas-flow interaction region.

In addition to their relative magnitude, the fluctuation signals are characterized in terms of their frequency spectra. Figure 3(d) shows the frequency-domain counterpart to the temporal signals in figure 3(c). The power spectrum is obtained by normalizing the product of the Fourier domain data and its complex conjugate with the sample size. From figure 3(d), four main peaks are observed for

the Upstream condition, i.e. f_{p1} = 9.5, f_{p2} = 14.3, f_{p3} = 19.1, and f_{p4} = 26.2 kHz; and their corresponding power (amplitude) are: P_1 = 4.0, P_2 = 8.8, P_3 = 1.0, and P_4 = 55.3 K^2-Hz^{-1}, respectively. The low frequency peaks are usually due to large-scale variations, which are mostly closer to the fundamental frequency of the system. The higher frequency peaks correspond to small-scale property variations. The 4th peak frequency, i.e. f_{p4} = 26.2 kHz, shows that the frequency corresponding to the small-scale has the highest magnitude of the power spectrum (P_4 = 500 K^2-Hz^{-1}), at the Near-cathode region. The small-scale variation in T_h provides some notion into the sensitivity of the cathode attachment; particularly addressing the time-scale and the intensity at which the electromagnetic and the drag forces continuously balance each other. Thus, to effectively analyze the plasma flow dynamics, adequate resolution of small-scale signals, as well as appropriate handling of the coupling among large- and small-scales is necessary. The use of the non-linear VMS (VMS$_n$) method aims to address these requirements, as described next.

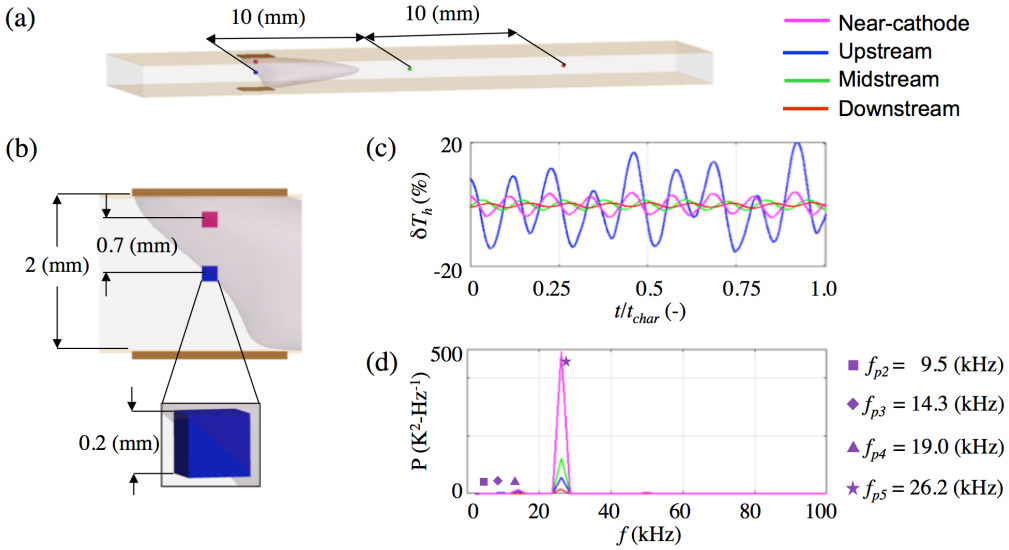

Figure 3. Assessment of flow dynamics: Placement of observation-points along the (a) axial direction and (b) near the cathode, as well as the spatial extent of each point; (c) representative fluctuation signals, given as percentages with respect to the mean value, for the heavy-species temperature; and (d) power spectrum in the frequency domain, indicating the dominant (peak) frequency of the signals.

4.3. Role of the numerical solution approach

Numerical methods for thermal plasma flow simulations need to be *robust* in order to deal with the marked non-linearity of the associate models, as well as *accurate* in order to resolve the multi-scale characteristics of the solution fields, particularly if the aim is to describe dynamic and unstable behavior. The VMS method, although it has been satisfactorily applied to various plasma flow simulations [12, 27, 31, 35, 37, 49], it is not inherently suitable for the description of multiscale phenomena in which the small- and large- scales interact in a highly-coupled and nonlinear manner, as it is the case in turbulent and instability phenomena. The non-linear VMS method presented in section 2.2 (i.e. VMS$_n$) addresses up-front the non-linearity of the coupling between small- and large-scales. The VMS$_n$ method has been successfully applied to representative incompressible and compressible laminar and turbulent flow simulations, and to the simulation of the flow from non-transferred arc plasma torches [42]. Therefore, the VMS$_n$ method is also expected to provide a more accurate description of the dynamic behavior in the arc in crossflow than the VMS method.

Figure 4 presents a representative comparison between the results obtained with the VMS and VMS$_n$ methods for the same conditions used in figure 2 (*left*), strong-flow – weak-arc (Re = 8630 and Π_I = 85.4). The simulations were run until a (fluctuating) steady-state is achieved in all solution fields, i.e. moving time-averaged quantities ($\overline{T}_h$, $\overline{T}_e$, $\overline{\phi}_p$, etc.) remain constant in time. Temporal fluctuation signals and power spectra for electric potential are shown figure 4(a), for heavy-species temperature in figure 4(b), and for electron temperature in figure 4(c) for each of the four observation-points (i.e. Near-cathode, Upstream, Midstream and Downstream).

The comparison shows the relative effectiveness of the VMS and VMS$_n$ methods for capturing dynamic behavior. Specifically, the results in figure 4 show that the fluctuation signals obtained with the VMS$_n$ method are more uniform (periodic) than those obtained with VMS. The electric potential fluctuations presented in figure 4(a) show the more uniform periodicity of the VMS$_n$ results with respect to those from VMS, which are quantified by the different peaks in the frequency-domain signals. The VMS method results show five frequency peaks, i.e. f_{p1} = 5.6, f_{p2} = 9.4, f_{p3} = 13.2, f_{p4} = 18.9 and f_{p5} = 22.6 kHz, with power $P_1 = 3.5 \cdot 10^{-4}$, $P_2 = 8.7 \cdot 10^{-5}$, $P_3 = 2.1 \cdot 10^{-5}$, $P_4 = 1.1 \cdot 10^{-3}$ and P_5 =

$2.2 \cdot 10^{-3}$ V^2-Hz^{-1}, respectively, for the Near-cathode region. In contrast, the VMS$_n$ method shows only four peaks (named from 2nd to 5th for consistency with the VMS results), which are closely comparable to the peaks obtained from VMS method. The power of the 2nd, 3rd, and 4th peaks obtained using the VMS$_n$ method are remarkably low compared to those obtained with VMS. The 3rd frequency peak (P_3) of electric potential has lesser power (both in VMS and VMS$_n$) compared to the other peaks (2nd, 4th, etc.). The results show that the 5th frequency peak (P_5) obtained using the VMS method is comparable to the 5th peak obtained using the VMS$_n$ method. The significant magnitudes of the 1st and 4th frequency peaks obtained with the VMS method are not seen in VMS$_n$ results.

The spectra of the electric potential fluctuations (figure 4(a)) are comparable to those for the heavy-species temperature (figure 4(b)) and the electron temperature (figure 4(c)). The time-domain fluctuations of T_h obtained with the VMS method (figure 4(b) *left*) are quasi-periodic, whereas those obtained with VMS$_n$ (figure 4(b) *right*) are smooth and periodic. Although the peak frequencies of the fluctuations are approximately the same for ϕ_p, T_h, and T_e, their corresponding power is significantly different. This is expected given that the magnitude of ϕ_p is ~ $O(10^1)$, whereas for T_h, and T_e ~ $O(10^3$-$10^4)$. Comparing the power spectra in figure 4(b), one can quantitatively assess the difference between the results from the VMS and the VMS$_n$ methods. The 2nd peak (P_2) and the 3rd peak (P_3) are comparable in magnitudes between the two methods (VMS and VMS$_n$), i.e., for the Near-cathode region, P_2 = 1.5 and 4.8 K^2-Hz^{-1} and P_3 = 12.6 and 9.0 K^2-Hz^{-1}, for VMS and VMS$_n$; whereas the 5th peak (P_5) is remarkably different, i.e. P_5 = 87.0 and 491.4 K^2-Hz^{-1} obtained using VMS and VMS$_n$ respectively. This marked deviation in peak frequency can be analyzed considering that the low (fundamental) frequency peak corresponds to the large-scale variations and the high frequency peaks correspond to the small-scale variations; hence, the sequence $f_{p1} > f_{p2} > f_{p3} > f_{p4} > f_{p5}$ can be correlated to the resolution from large-scales to progressively smaller-scales. The relative agreement $P_{2VMS} \approx P_{2VMSn}$ and $P_{3VMS} \approx P_{3VMSn}$ indicates that VMS$_n$ can capture all the large-scales variations similarly as VMS; whereas observed $P_{5VMS} << P_{5VMSn}$ indicates that VMS$_n$ captures the small-scales significantly more accurately than VMS. Given the large power of the frequency signals at the arc-gas interface (i.e., both, the Near-cathode and the Upstream locations),

it can be concluded that the VMS$_n$ provides a better description of arc – gas flow interactions than VMS. This finding motivates the use of the VMS$_n$ method for the identification of flow regimes.

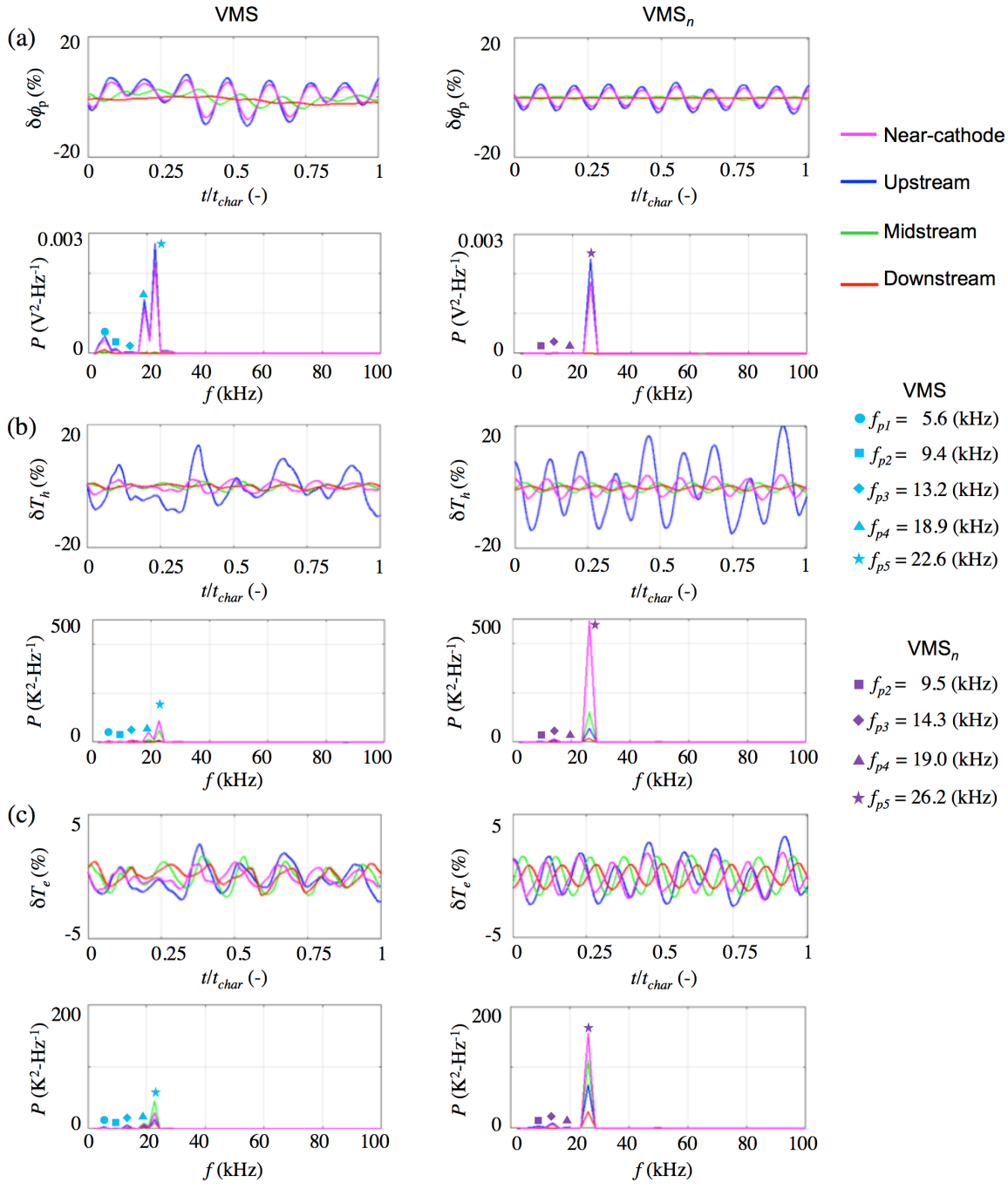

Figure 4. Comparison of arc fluctuation results obtained with the (*left column*) VMS and (*right column*) VMS$_n$ methods for: (a) electric potential ϕ_p, (b) heavy-species temperature T_h, and (c) electron temperature T_e; (*top frames*) percentage change (δ) with respect to the mean temporal value in the time domain and (*bottom frames*) signal power (P) in the frequency domain.

5. Arc characteristics and regimes of the arc in crossflow

5.1. Arc shape and characteristics

The arc shape and the arc behavior are the result of the energy balance between the supplied electrical energy (Joule heating) and the energy lost as a result of convective cooling to the stream of working gas. The phenomenological characterization of the arc in crossflow with respect to the arc shape was presented in [11] through the computational simulations of 19 cases for the range of Reynolds and the Enthalpy dimensionless numbers, $0 < Re < 10000$ and $2 < \Pi_I < 350$. As part of the present research, the arc shape (figure 5) and the arc characteristics (figure 6) were obtained for an extended Re-Π_I range (i.e. $0 < Re < 10000$ and $50 < \Pi_I < 800$).

Consistent with experimental and numerical studies of the arc in crossflow [11, 29, 45], the arc shape changes from cusp- to bow- shaped for increasing Re and decreasing Π_I, resulting in increased arc length (e.g., figure 5: case B_1 to case D_1 or B_4 to case D_1) and increased electric potential (figure 6(a)). For increasing Re and Π_I (figure 5: case B_1 to case D_4), the arc temperature (figure 6(b)) and arc power (figure 6(c)) increases due to strong electromagnetic pumping. The overall increase in arc temperature leads to large temperature gradients as well as increased local acceleration across the electrodes. The variation of Re and Π_I among the cases are accommodated by modifying the inlet velocity $U_{i\max}$ (i.e. from 1.2 to 117.0 m-s^{-1}) and the imposed current I_{tot} (i.e. from 16 to 657 A).

The time-step size for all the cases (B1 to D4) is of the order $O(10^{-6})$ to $O(10^{-7})$, similar to our previous works [11, 17], except for the high Reynolds and low Enthalpy number cases (e.g. D1) for which the time step is in the order of $O(10^{-8})$. The smaller timestep size was necessary due to the large elongation and the highly dynamic nature of the arc. Additionally, the case D1 involved a greater number of timesteps to obtain a converged solution.

The controlling parameters Re and Π_I determine not only the overall arc shape but also the arc behavior (i.e. the characteristics of property fluctuations). The effects of the Reynolds and the Enthalpy numbers on the arc behavior are analyzed next.

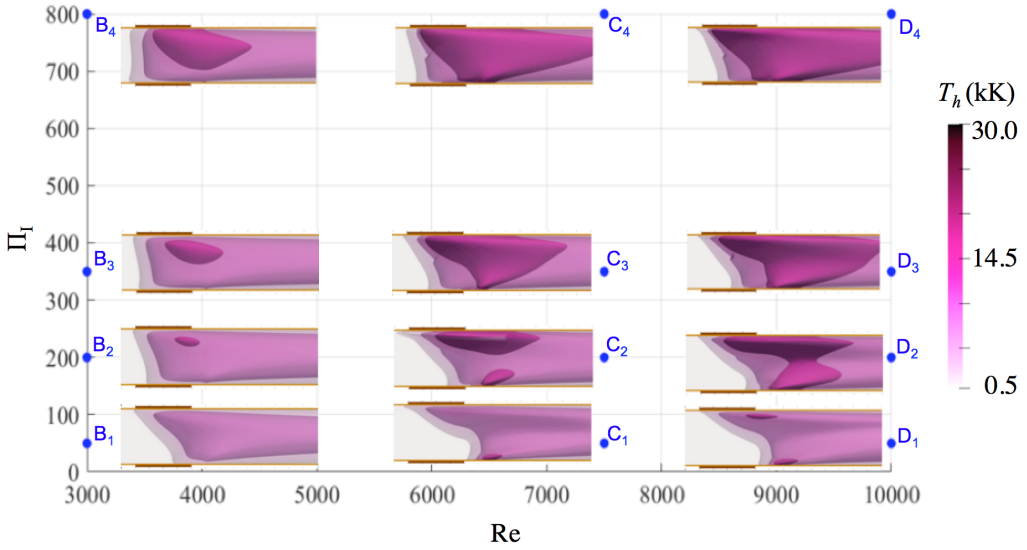

Figure 5. Arc shape characterization: iso-surfaces of T_h = 2, 8, 15, 20 (kK) as function of the Reynolds number *Re*, and the Enthalpy number Π_I. The blue dots indicate the values used in the simulations.

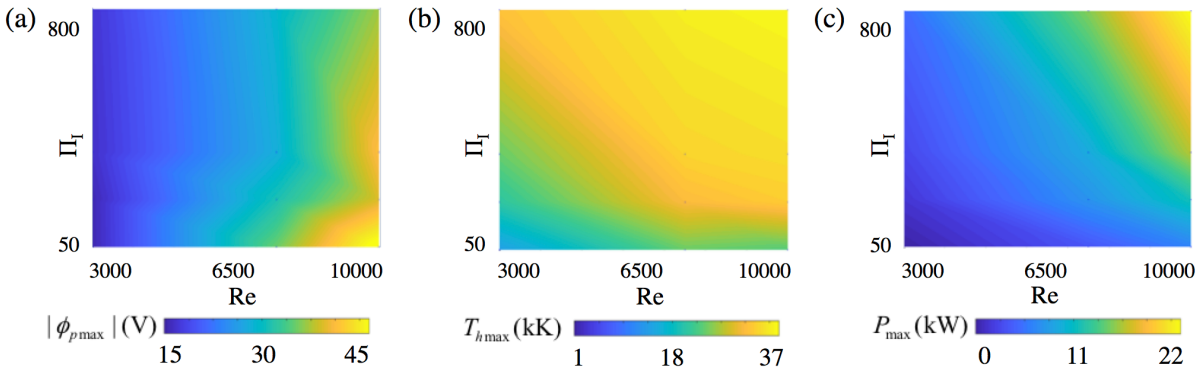

Figure 6. Arc in crossflow characteristics: (a) maximum voltage drop $|\phi_{p\max}|$, (b) maximum heavy-species temperature $T_{h\max}$, and (c) arc power $P_{\max}$.

5.2. Effect of Reynolds and Enthalpy numbers on the arc dynamics

The characteristics of the arc as function of the Reynolds number are depicted in figure 7 and those as obtained as function of the Enthalpy number in figure 8. Figure 7 (*left*) shows that the arc evolves towards having an anode attachment further downstream with increasing *Re*. The magnitude and frequency of the temporal fluctuations of T_h also increase with increasing *Re*, as depicted in figure 7 (*center*). The fluctuations change from steady (figure 7(a)), to quasi-periodic (figure 7(b)), and then

to near-periodic with higher amplitudes (figure 7(c)). The increased characteristic fluctuations with increasing *Re* results in an increase in the number of peak frequencies [21] and an increase in the magnitude of their power, as seen in right of figure 7 (*right*). Low *Re* simulations are characterized by the presence of a single frequency peak due to negligible variation temporal fluctuations (i.e., in figure 7(a), for $Re = 3000$, $\delta T_h < 1\%$ and $f_{p1a} = 1.3$ kHz); and the amplitude fluctuations and the number of peak frequencies increase with *Re* (i.e., for $Re = 7500$ (figure 7(b)), $\delta T_h \approx \pm 13\%$ and presents two dominant frequencies: $f_{p2a} = 11.1$ and $f_{p2a} = 20.6$ kHz; and for $Re = 10000$ (figure 7(c)), $\delta T_h \approx \pm 25\%$ and presents four dominant frequencies: $f_{p3a} = 13.2$, $f_{p3b} = 26.4$, $f_{p3c} = 37.7$ and $f_{p3d} = 49.0$ kHz). The increase in the number of dominant frequencies indicates the increasing complexity of the temporal fluctuations, and hence of characteristic temporal scales (each scale given by the inverse of a characteristic frequency), as well as spatial (small-) scales (associated to the amplitude of the fluctuations).

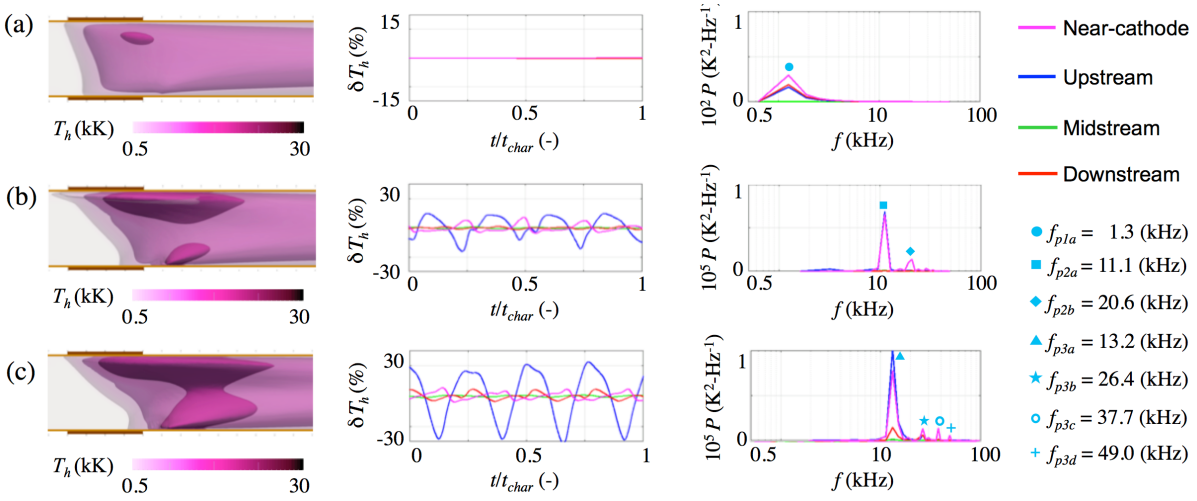

Figure 7. Effect of the Reynolds number on the arc in crossflow: (*left*) distribution of heavy-species temperature T_h, (*center*) fluctuations with respect to the temporal-mean value, and (*right*) power spectra of the fluctuations; conditions: $\Pi_I = 50$ and *Re* = (a) 3000, (b) 7500, and (c) 10000.

Additionally, at low Reynolds number (i.e. $Re = 3000$, figure 7(a) *right*), the power of the fluctuation signals in the Near-cathode region is higher than at any other locations (e.g. $P_1 = 29.3$ and

16.2 K^2-Hz^{-1} at the Near-Cathode and Upstream regions, respectively). However, for increasing Reynolds, the power of the fluctuation signals increases at the Upstream observation-point and surpasses the fluctuations at the Near-cathode at higher Reynolds (i.e. $P_2 = 6.8 \cdot 10^4$ and $6.6 \cdot 10^4$ K^2-Hz^{-1}, $P_3 = 7.8 \cdot 10^4$ and $10.2 \cdot 10^4$ K^2-Hz^{-1}; at the Near-Cathode and Upstream regions, respectively). The strong fluctuation at the Upstream observation-location is due to the downstream arc anode attachment and the strong nonequilibrium at the plasma – gas interface.

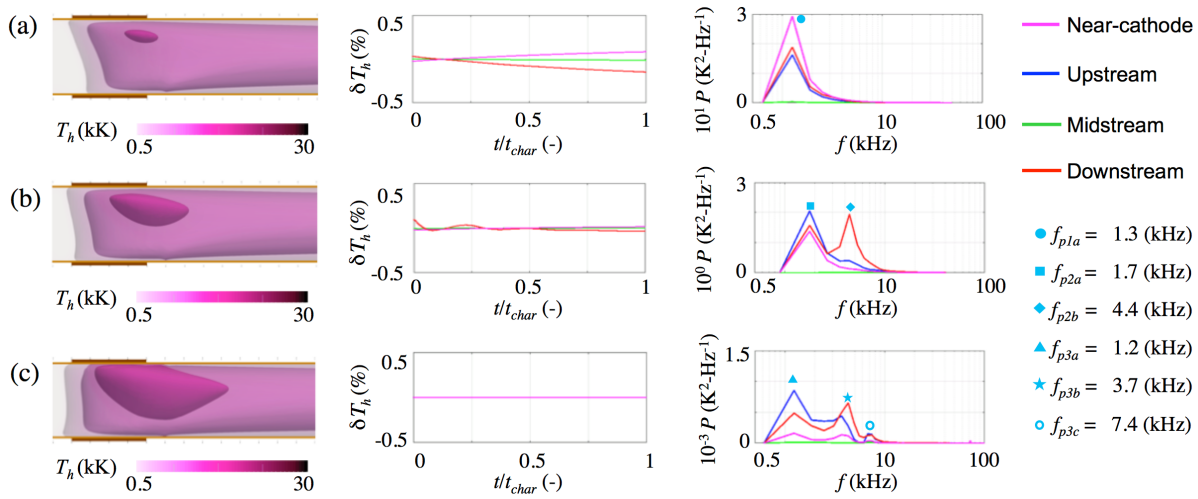

Figure 8. Effect of the Enthalpy number on the arc in crossflow: (*left*) distribution of heavy-species temperature T_h, (*center*) fluctuations with respect to the temporal-mean value, and (*right*) power spectra of the fluctuations; conditions: Re = 3000 and Π_I = (a) 200, (b) 350, and (c) 800.

The results in figure 8 show that with increasing Enthalpy number, the anode attachment moves upstream, the arc shape changes from bow- to cusp-shaped (i.e., the arc gets bulgy), and the amplitude and frequency of fluctuations decrease (i.e. figure 8(a) to (c), δT_h reduces from ±0.5% to an insignificant value), and hence the arc becomes relatively more stable. The relative arc stability can be assessed by observing the frequency spectra, where the power of the signals gets reduced drastically, by over 4 orders of magnitudes, with increasing Π_I (i.e. $P_1 = 29.3$, 16.2, 18.9 K^2-Hz^{-1}; $P_2 = 0.4$, 1.6, 1.4 K^2-Hz^{-1}; and $P_3 = 1.6 \cdot 10^{-4}$, $8.6 \cdot 10^{-3}$, $4.9 \cdot 10^{-3}$ K^2-Hz^{-1} at the Near-cathode, Upstream, and Downstream observation-points, respectively; the subscripts 1, 2 and 3 correspond to Π_I = 200, 350

and 800, respectively). The drastic decrease in the power of the signals indicates the establishment of an increasingly stable configuration of the plasma, and the signals can be considered as *white noise*.

At higher Reynolds, increasing the Enthalpy number increases arc stability but also increases the maximum arc temperature (figure 6(b)) and the overall arc power (figure 6(c)). The increase in the arc temperature causes large temperature gradients, especially in the region near the cathode (e.g., see figure 5, case D4). To effectively study arc dynamics at high *Re* and Π_I, the grid resolution should be fine enough to appropriate resolve the associated large gradients present in the solution fields. The use of a finer discretization in the present study compared to the one used in our previous study [11] has significantly improved the convergence of the numerical simulations. Nevertheless, use of the finer grid resulted in a significant increase in computational cost (~1.5 to 2 times greater than in [11]). The present study indicates that the magnitude of the peak frequencies (f_p) and the increase in the number of peak frequencies with Reynolds number (e.g. from 1 for Re = 3000 to 4 for Re = 10000, as seen in figure 7) for the studied *Re*-Π_I range is grid independent, and that even finer discretizations are required to analyze the arc in crossflow for a wider *Re*-Π_I range.

5.3. Spatiotemporal fluctuations and regimes identification

The dynamics of the arc in cross flow as function of the Reynolds and Enthalpy numbers can be summarized using three quantities: the time-averaged values, the peak frequency of fluctuations, and the variance of those fluctuations. These quantities are presented in figures 9 to 10 for ϕ_p, T_h, and T_e as representative flow properties, and for each observation-point.

Figure 9 presents the variation of the time-averaged electric potential $\overline{\phi}_p$, heavy-species temperature $\overline{T}_h$, and electron temperature $\overline{T}_e$ as function of *Re* and Π_I at each observation-point (i.e. Near-cathode, the Upstream, the Midstream and the Downstream). These quantities are defined using a moving-average procedure, i.e. $\overline{\phi}_p$ for a given observation-point is defined by:

$$\overline{\phi}_p(\mathbf{x}_{op}) = \frac{1}{\Delta t_f} \int_{t_f-\Delta t_f}^{t_f} \phi_p(t, \mathbf{x}_{op})\, dt, \tag{10}$$

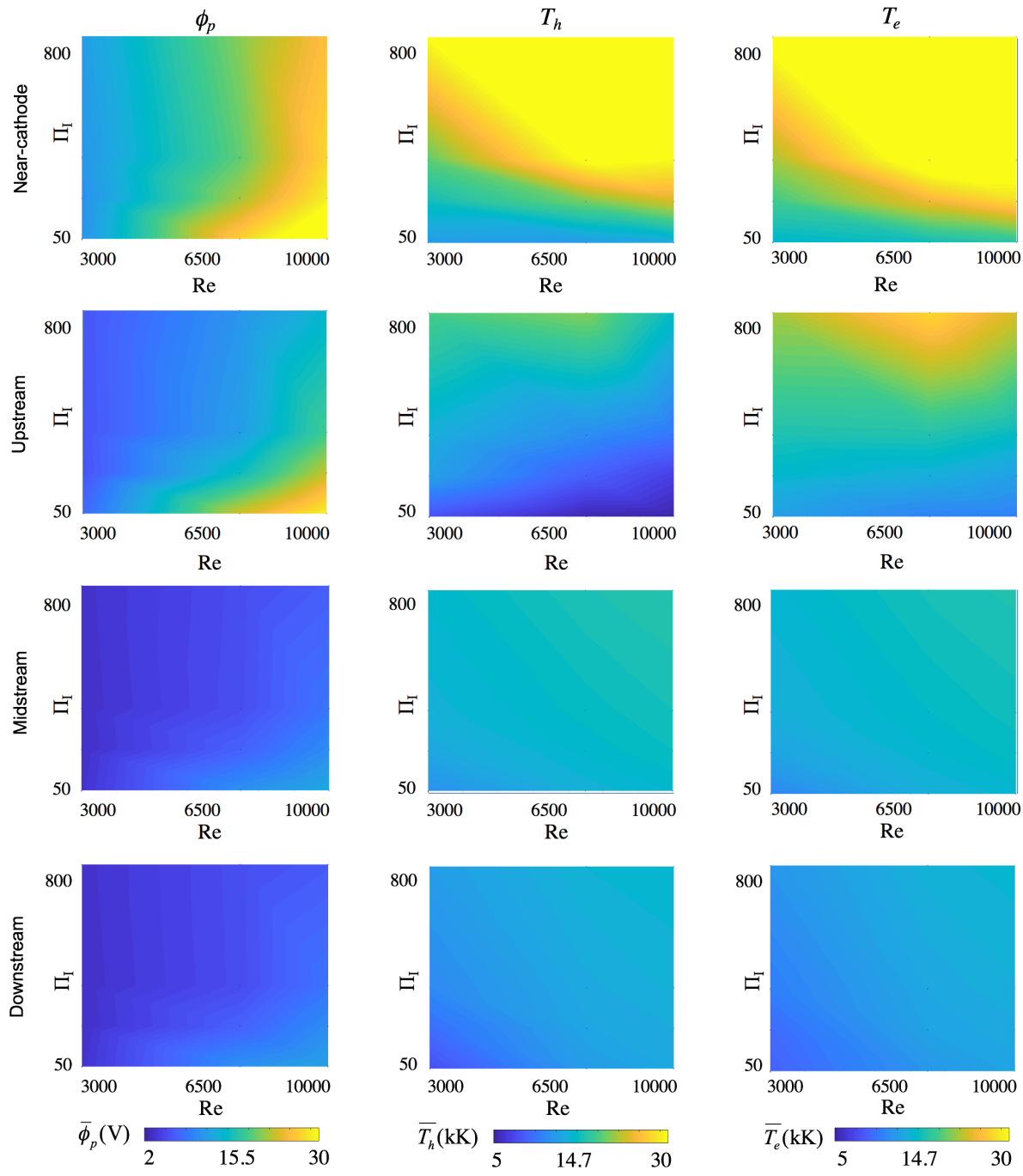

Figure 9. Effect of the Reynolds and the Enthalpy numbers on the average electric potential, heavy-species temperature, and electron temperature at each observation-point.

where $\mathbf{x}_{op}$ represents the spatial location of the given observation-point, t_f is the final time of the simulation ($t_f >> t_{char}$), and Δt_f is an arbitrary time interval used for the analysis such that $\Delta t_f > t_{char}$. The expression in Eq. (10) is evaluated for a temporal extent that ensures that steady-state has been

achieved such that $d\overline{\phi}_p / dt = 0$ independently of the specific value of Δt_f. Similar expressions are used to define $\overline{T_h}$ and $\overline{T_e}$.

In figure 9, it can be observed that for high *Re* and low Π_I (i.e. near case D_1, see figure 5) at the Near-cathode location, $\overline{\phi_p}$ is maximum (i.e. 33.8 V), as expected due to the large arc length (consistent with the maximum electric potential distribution in figure 6(a)). This implies that the high energy loss by advective cooling has to be compensated by greater electrical energy consumption. Also, at this point $\overline{T_h}$ is minimum (i.e. 12.2 kK) due to the strong cooling; whereas, $\overline{T_e}$ remains largely unaffected with varying *Re* for the same value of Π_I (i.e. 16.4 kK).

For high *Re* and Π_I, also at the Near-cathode location, $\overline{T_e}$ increases due to strong Joule heating (i.e. ~ 37 kK for case D_4 in figure 5). At the Upstream location, the values of $\overline{\phi_p}$ and $\overline{T_h}$ are similar to those at the Near-cathode location, whereas the $\overline{T_e}$ distribution remains unaffected for increasing *Re*. At the Midstream and the Downstream observation-points, the distributions of $\overline{\phi_p}$, $\overline{T_h}$, and $\overline{T_e}$ are somewhat analogous to their corresponding instantaneous maxima (depicted in figure 6). The distributions of the maximum heavy-species temperature $T_{h\max}$ (figure 6(b)) and the average heavy-species temperature $\overline{T_h}$ at the Midstream and the Downstream (figure 9) are analogous to the power distribution (figure 6(c)), which indicates that the increase in arc power increases the overall temperature. In contrast, the heavy-species in the Near-cathode and the Upstream locations undergo drastic reductions in temperature due to the strong interaction with the gas flow stream. The reduction in T_h is a result of the strong cooling of the arc by the gas flow, and the increased degree of nonequilibrium, which can potentially lead to turbulence [13].

The phenomenon of abrupt drop in the heavy-species temperature with increasing *Re* and for low values of Π_I (figure 9, Upstream and Near-cathode observation-points) is somewhat analogous to the drastic reduction in the plasma jet length in a non-transferred plasma torch due to the increase in gas flow rate, which results in the transition from laminar to turbulent flow [22, 50, 51]. This behavior can be better understood by inspecting the frequency and variance of fluctuations.

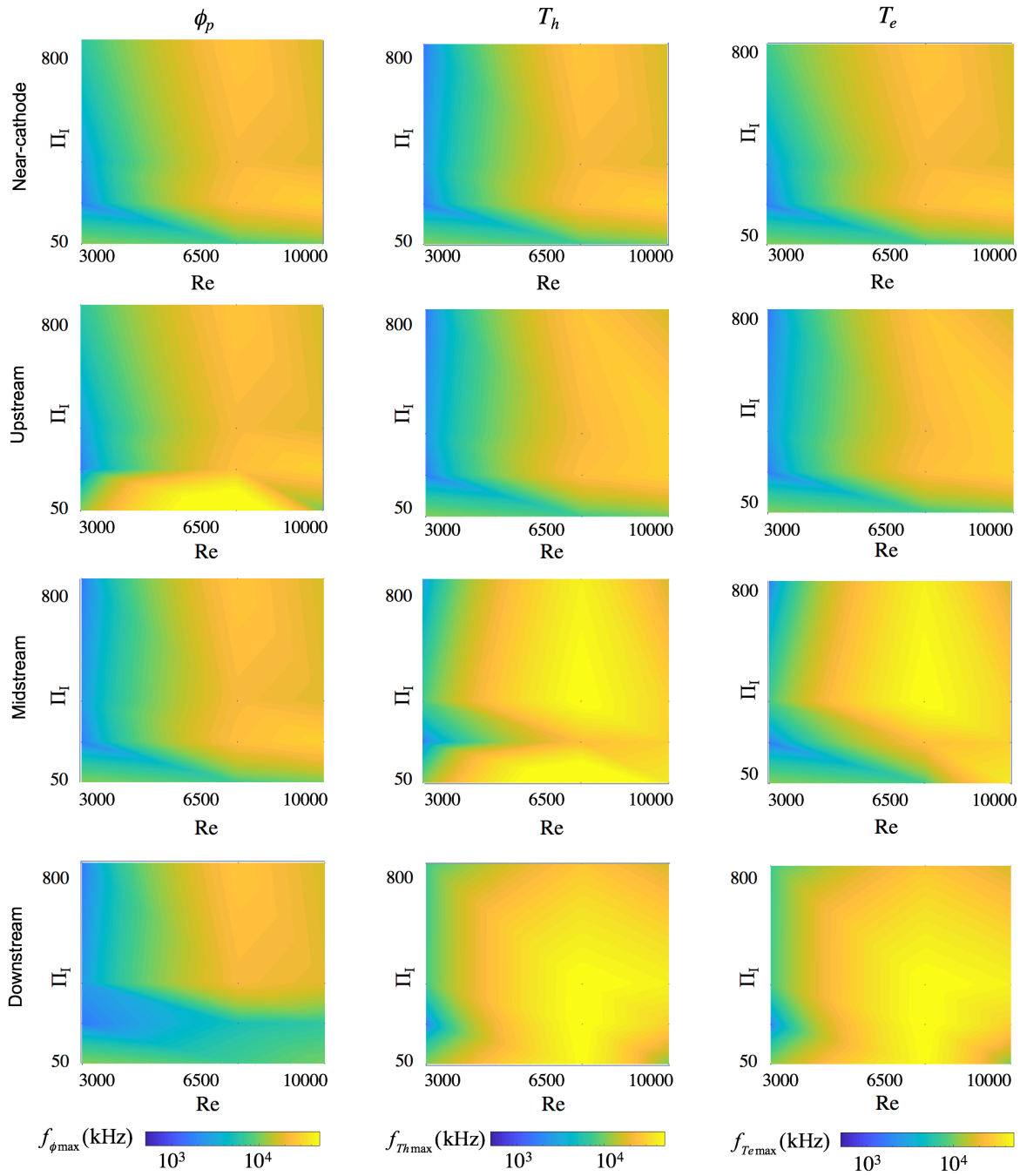

Figure 10. Effect of the Reynolds and the Enthalpy numbers on the peak frequency of the fluctuations in electric potential, heavy-species temperature, and the electron temperature at observation-points.

Figure 10 presents the variation of the peak frequency $f_{\max}$ of the fluctuations electric potential, heavy-species, and electron temperatures as function of *Re* and Π_I at each observation-point. The peak frequencies correspond the frequencies with the highest power, e.g. as shown in figures 7 and 8.

In the Near-cathode region, for increasing *Re*, the peak frequencies increase by ~ 1 to 2 orders of magnitude, whereas increasing Π_I at constant *Re*, the relative change in peak frequency is subtle. This is somewhat consistent with observations in plasma torches [19], in which the peak frequency of voltage fluctuations increases mostly with increasing gas flow and varies little with increasing total current. The peak frequencies of T_h and T_e in the Upstream location are similar to those at the Near-cathode. These peak frequencies increase when moving downstream (i.e., from the Upstream, to the Midstream, and then to the Downstream observation-points). In contrast, no significant change is observed for ϕ_p among the different observation-points.

The observed trends for the peak frequency f_{max} of the fluctuations as function of *Re* and Π_I have to be contrasted against their amplitude. In this regard, figure 11 presents the distribution of the variance s^2 of the fluctuations of electric potential, heavy-species temperature, and electron temperature as function of *Re* and Π_I at each observation-point.

The variance quantifies the squares of the amplitudes of the fluctuation signals. Specifically, the variance of the electric potential ϕ_p is given as:

$$s_{\phi}^2(\mathbf{x}_{op}) = \frac{1}{\Delta t_f} \int_{t_f - \Delta t_f}^{t_f} (\phi_p(t, \mathbf{x}_{op})^2 - \bar{\phi}_p(\mathbf{x}_{op})^2) dt. \tag{11}$$

Similar expressions are used for the variances of heavy-species and electron temperatures.

It is to be noted that the variance plots in figure 11 are significantly non-smooth, showing distinct faceted regions. Non-smoothness of the distributions of peak frequency with *Re* and Π_I can also be observed in the results in figure 10, but to a lower degree. The lack of smoothness in s^2 is the results of the very limited amount of points used to probe the *Re* - Π_I map (i.e. 12 points, as indicated in figure 5). The small number of *Re* - Π_I sets studied is due to the large computational cost of the simulations, each involving the fully-coupled solution of the 10-variable equations-set given by Eq. (1), for a total of ~ 2.5 million unknowns and for over ~ 6000 time steps (~ 0.1 to 3.0 μs) after achieving steady-state, and requiring approximately 5 weeks of computing time per case using 16 Intel E5-2600 cores.

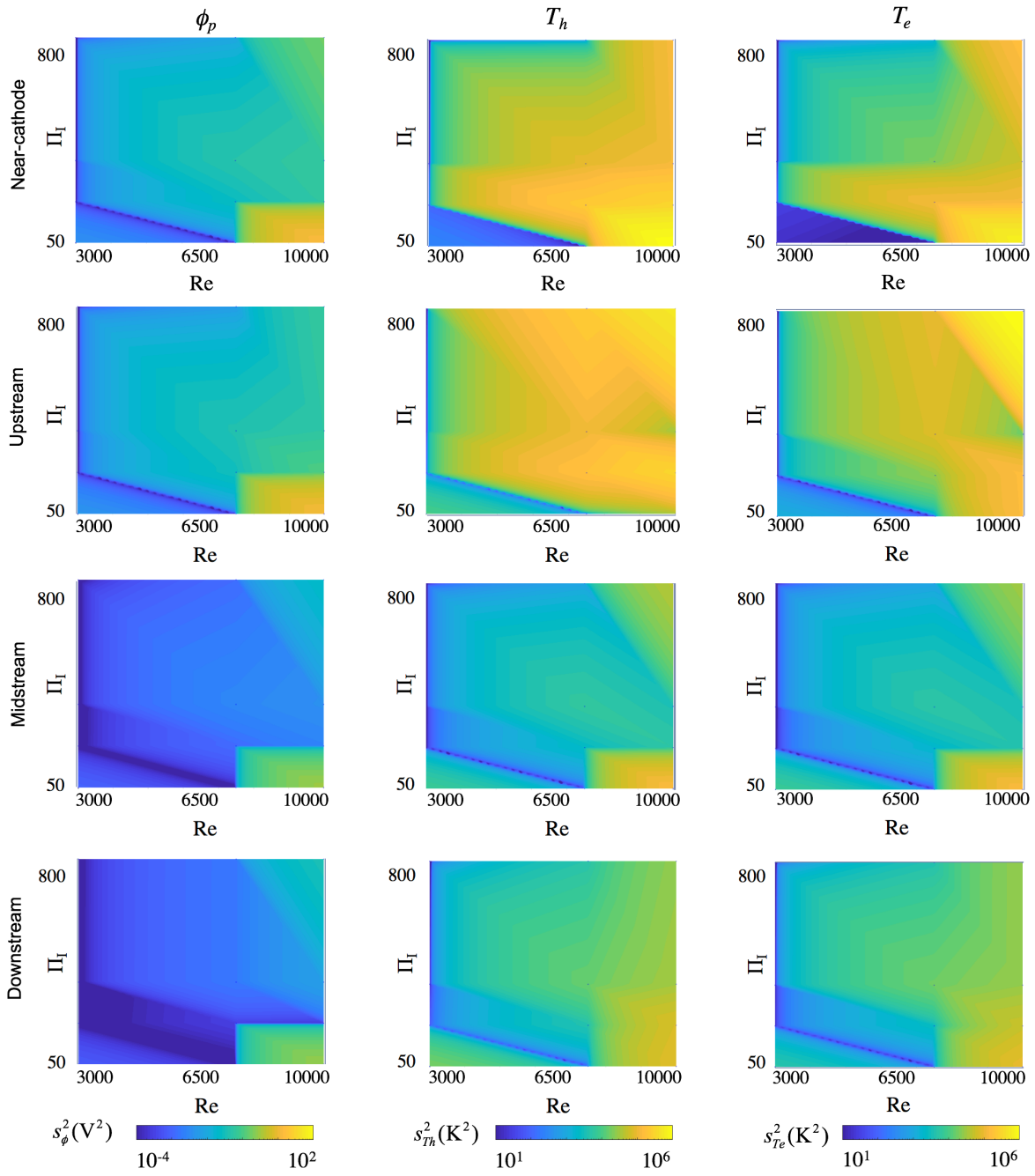

Figure 11. Effect of the Reynolds and the Enthalpy numbers on the variance of the fluctuations in electric potential, the heavy-species temperature, and electron temperature at the observation-points.

The magnitudes of s^2_ϕ compared to those of s^2_{Th} and s^2_{Te}, as shown in figure 11, indicate that the fluctuations in electric potential are significantly smaller than those for the heavy-species and electron temperatures (i.e., the former vary from $O(10^{-4})$ to $O(10^{2})$, whereas the latter, from $O(10^{1})$ to $O(10^{6})$).

This can be expected given that temperatures distributions are more dependent on the plasma flow (e.g. heat generated by Joule heating versus heat loss by convection) than the electric potential distribution (which depends mostly on the electrodes configuration and total imposed current). Additionally, of s_{Th}^2 and s_{Te}^2 rapidly increase with increasing *Re* and Π_I at the Near-cathode and Upstream observation-points, whereas the slowly increase with increasing *Re* and Π_I at the Midstream and the Downstream locations.

The distributions of peak frequency (figure 10) and variance (figure 11) of the heavy-species temperature fluctuations at the Midstream and Downstream observation-points suggest they strongly correlate with the arc dynamics and the degree of plasma – gas flow interaction. Between these two locations, the Midstream observation-point remains more consistently within the bulk plasma, and it is therefore preferred for the assessment of flow characteristics. Therefore, $f_{Th\max}$ and of s_{Th}^2 can be used to assist in determining characteristic regimes of the arc in crossflow. These quantities are employed to determine the regimes of the arc in crossflow, as shown in figure 12.

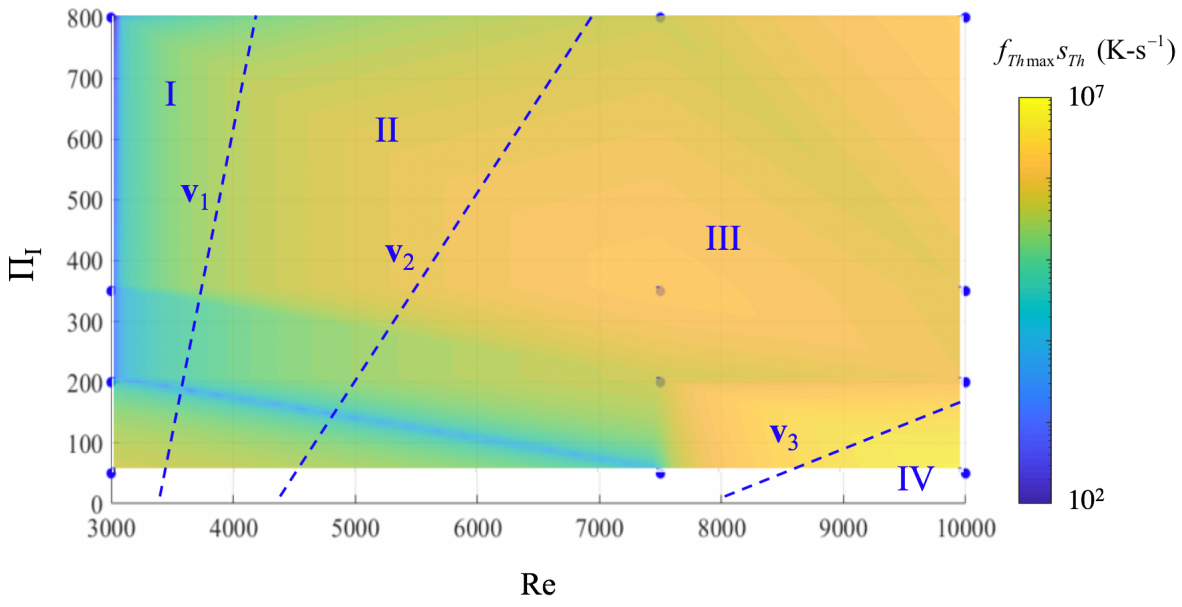

Figure 12. Approximate extent of distinct flow regimes in the arc in cross flow: Regions with distinct characteristics of the metric $f_{Th\max}s_{Th}$ as delineated by lines $\mathbf{v}_1$, $\mathbf{v}_2$, and $\mathbf{v}_3$: I – steady, II – periodic, III – quasi-periodic, IV – chaotic.

Figure 12 shows the distribution of the product $f_{Th\max} s_{Th}$, where $s_{Th} = (s_{Th}^2)^{\frac{1}{2}}$ is the standard deviation, at the Midstream observation-point, which is used as a metric for regime identification. The results in figure 12 show the regions delineating four distinct flow regimes in the *Re*- Π_I map, i.e.: I – static, II – periodic, III – quasi-periodic, and IV – chaotic. These regions approximately present different characteristics in terms of the frequency of fluctuations and their magnitude: region I – static present low-frequency fluctuations and of very small magnitude; region II – periodic, presents well-defined fluctuations of higher frequency and amplitude; region III – quasi-periodic, presents more fluctuations, with several peaks in the frequency-domain, and increased amplitude of fluctuations; and finally, region IV- chaotic, shows more complex frequency-domain signals and of greater amplitude. The transition from a laminar to a (potentially) turbulent regime of the arc in crossflow occurs from region II to region III (can be termed as the laminar – turbulent transition region) or region IV; and is governed by both the Reynolds number and the Enthalpy number. It is to be noted that region IV comprises only one set of results (i.e. case D_1 in figure 5). This simulation was significantly more computationally expensive compared to the others in terms of the large number of non-linear iterations per time-step required for convergence and the large number of time-steps needed to achieve steady-state. Such behavior in a numerical simulation is often indicative of the onset of instability and potentially turbulent behavior [34], which require significantly higher spatial and temporal resolution for their description (i.e. finer grid and smaller time steps). Nevertheless, for consistency, the simulation of case D_1 used the same discretization grid as for all the other cases (i.e. 250k nodes).

The approach used to delineate the regions for each regime is similar to that used in [51], and consists on the determination of the separation lines $\mathbf{v}_1$, $\mathbf{v}_2$, and $\mathbf{v}_3$. These lines express the Enthalpy number as function of the Reynolds number, and each line is of the form:

$$\mathbf{v}_k : \quad \Pi_I = \alpha_k \, \mathrm{Re} + \beta_k, \tag{12}$$

where k indicate the index of the line (k = 1, 2, or 3); and α and β are coefficients defining the line,. The extent of each regime can be determined for a given set of Re and Π_I as:

$$
\begin{aligned}
&\text{I (static)}: && \alpha_1 \,\mathrm{Re} + \beta_1 < \Pi_I \\
&\text{II (periodic)}: && \alpha_2 \,\mathrm{Re} + \beta_2 < \Pi_I < \alpha_1 \,\mathrm{Re} + \beta_1 \\
&\text{III (quasi-periodic)}: && \alpha_3 \,\mathrm{Re} + \beta_3 < \Pi_I < \alpha_2 \,\mathrm{Re} + \beta_2 \\
&\text{IV (chaotic)}: && \Pi_I < \alpha_3 \,\mathrm{Re} + \beta_3
\end{aligned}
\tag{13}
$$

Even though the followed approach is at most approximate for the identification of distinct flow regimes (i.e. there are not unambiguously distinct regions in the distribution of $f_{Th\max} s_{T_h}$ through the *Re*- Π_I map), a distinct advantage of it is that the approach could be adopted experimentally, i.e. by recording in-situ spatial-temporal data of heavy-species temperature at a location downstream from the electrodes yet within the bulk arc plasma.

6. Summary and conclusions

The flow dynamics and the establishment of different flow regimes in the arc in crossflow are studied using a 3D time-dependent NLTE plasma flow model. A nonlinear Variational Multiscale (VMS_n) numerical discretization approach is used to describe the coupling between the large- and small-scale features of the flow, providing greater numerical accuracy than traditional VMS methods. The Reynolds number and the Enthalpy number are used as control parameters. The dynamic behavior of the flow is characterized using the property variations gathered at four representative observation-points: one near the cathode, and three along the main axis for the flow. The time-averaged values of the temporal signals, as well as the frequency and variance of the signals fluctuations, are used to quantify the flow dynamics. The product of the standard deviation and the peak frequency of the heavy-species temperature at the midstream observation-point is used to identify the distinct regimes, i.e. steady, periodic, quasi-periodic, and chaotic. The computational results reveal the role of increasing the relative arc strength on enhancing flow stability by delaying the growth of fluctuating and unstable flow behavior.

Acknowledgments

The authors gratefully acknowledge support from the U.S. National Science Foundation through award CBET-1552037 and the U.S. Department of Energy through award DE-SC0018230.

References

1 N. A. Hussary and J. V. R. Heberlein, Journal of Thermal Spray Technology, **10**, 604, (2000).

2 E. Nogues, M. Vardelle, P. Fauchais, and P. Granger, Surface and Coatings Technology, **202**, 4387, (2008).

3 T. Watanabe, X. Wang, E. Pfender, and J. Heberlein, Thin Solid Films, **316**, 169, (1998).

4 I. Gedzevicius and A. V. Valiulis, Journal of Materials Processing Technology, **175**, 206, (2006).

5 E. Pfender, Plasma Chemistry and Plasma Processing, **19**, 1, (1999).

6 S. Ghorui, K. C. Meher, R. Kar, N. Tiwari, and S. N. Sahasrabudhe, Journal of Physics D: Applied Physics, **49**, 295201, (2016).

7 P. Fauchais and A. Vardelle, Plasma Physics and Controlled Fusion, **42**, B365, (2000).

8 F. Yang, Y. Wu, M. Rong, H. Sun, A. B. Murphy, Z. Ren, and C. Niu, Journal of Physics D: Applied Physics, **46**, 273001, (2013).

9 B. Swierczynski, J. J. Gonzalez, P. Teulet, P. Freton, and A. Gleizes, Journal of Physics D: Applied Physics, **37**, 595, (2004).

10 R. Huang, H. Fukanuma, Y. Uesugi, and Y. Tanaka, Journal of Thermal Spray Technology, **21**, 636, (2011).

11 V. G. Bhigamudre and J. P. Trelles, Journal of Physics D: Applied Physics, **52**, 015205, (2018).

12 J. P. Trelles, Journal of Physics D: Applied Physics, **46**, 255201, (2013).

13 L. Niemeyer and K. Ragaller, Z. Naturforsch, **28a**, 1281, (1973).

14 M. Shigeta, Journal of Physics D: Applied Physics, **49**, 493001, (2016).

15 O. I. Yas'ko, Pure & Appl. Chem., **62**, 1817, (1990).

16 O. I. Yas'ko, J. Phys. D: Appl. Phys. , **2**, 733, (1969).

17 V. G. Bhigamudre and J. P. Trelles, 44th IEEE International Conference on Plasma Science (ICOPS), 1, (2017).

18 Z. Duan and J. Heberlein, Journal of Thermal Spray Technology, **11**, 44, (2002).

19 N. Singh, M. Razafinimanana, and J. Hlina, Journal of Physics D: Applied Physics, **33**, 270, (2000).

20 X. Li, J. Chu, P. Jia, L. Yang, B. Wang, and K. Wu, Journal of Applied Physics, **123**, 103303, (2018).

21 W. X. Pan, Z. Y. Guo, X. Meng, H. J. Huang, and C. K. Wu, Plasma Sources Science and Technology, **18**, 045032, (2009).

22 W. Pan, X. Meng, and C. Wu, Plasma Science and Technology, **8**, 416, (2006).

23 C. Wu and W. Pan, Theoretical and Applied Mechanics Letters, **1**, 024001, (2011).

24 X. Tu, B. G. Chéron, J. H. Yan, L. Yu, and K. F. Cen, Physics of Plasmas, **15**, 053504, (2008).

25 R. Huang, H. Fukanuma, Y. Uesugi, and Y. Tanaka, Journal of Thermal Spray Technology, **22**, 183, (2013).

26 J. J. Gonzalez, P. Freton, and A. Gleizes, Journal of Physics D: Applied Physics, **35**, 3181, (2002).

27 J. P. Trelles, C. Chazelas, A. Vardelle, and J. V. R. Heberlein, Journal of Thermal Spray Technology, **18**, 728, (2009).

28 D. M. Benenson, A. J. Baker, and A. A. J. Cenkner, IEEE Transactions on Power Apparatus and Systems, **88**, 513, (1969).

29 H. H. Maeckar and H. G. Stablein, IEEE Transactions on Plasma Science, **14**, 291, (1986).

30 A. Lebouvier, C. Delalondre, F. Fresnet, V. Boch, V. Rohani, F. Cauneau, and L. Fulcheri, IEEE Transactions on Plasma Science, **39**, 1889, (2011).

31 J. P. Trelles, J. V. R. Heberlein, and E. Pfender, Journal of Physics D: Applied Physics, **40**, 5937, (2007).

32 M. Kelkar and J. Heberlein, J. Phys. D: Appl. Phys. , **33**, 2172, (2000).

33 L. Lincun, X. Weidong, Z. Heling, and M. Qiang, Plasma Science and Technology, **9**, 564, (2007).

34 J. P. Trelles, Plasma Sources Science and Technology, **27**, 093001, (2018).

35 J. P. Trelles and S. M. Modirkhazeni, Comput. Methods Appl. Mech. Engrg., **282**, 87, (2014).

36 V. Colombo, E. Ghedini, M. Boselli, P. Sanibondi, and A. Concetti, Journal of Physics D: Applied Physics, **44**, 194005, (2011).

37 J. P. Trelles, Plasma Process Polymers, **14**, 1600092, (2017).

38 T. J. R. Hughes, G. R. Feijóo, L. Mazzei, and J.-B. Quincy, Computer Methods in Applied Mechanics and Engineering, **166**, 3, (1998).

39 R. Zanino, Journal of Computational Physics, **138**, 881, (1997).

40 G. E. Georghiou, R. Morrow, and A. C. Metaxas, Journal of Physics D: Applied Physics, **33**, 2453, (2000).

41 U. Shumlak, R. Lilly, S. Miller, N. Reddell, and E. Sousa, 19th IEEE Pulsed Power Conference (PPC), 1, (2013).

42 S. M. Modirkhazeni and J. P. Trelles, Journal of Thermal Spray Technology, **27**, 1447, (2018).

43 Y. Bazilevs, V. M. Calo, J. A. Cottrell, T. J. R. Hughes, A. Reali, and G. Scovazzi, Computer Methods in Applied Mechanics and Engineering, **197**, 173, (2007).

44 E. Moreau, C. Chazelas, G. Mariaux, and A. Vardelle, Journal of Thermal Spray Technology, **15**, 524, (2006).

45 D. M. Benenson and A. A. Cenkner Jr, Journal of heat transfer, **92**, 276, (1969).

46 H. Guo, X.-N. Zhang, J. Chen, H.-P. Li, and K. Ostrikov, Scientific Reports, **8**, 4783, (2018).

47 M. S. Benilov, J. Phys. D: Appl. Phys, **41**, 144001, (2008).

48 V. Colombo, E. Ghedini, and P. Sanibondi, Journal of Physics D: Applied Physics, **43**, 105202, (2010).

49 S. ModirKhazeni and J. Trelles, 22nd International Symposium on Plasma Chemistry (ISPC), Montreal, Canada, (2015).

50 K. Cheng, X. Chen, and W. Pan, Plasma Chemistry and Plasma Processing, **26**, 211, (2006).

51 X. Chen, W. Pan, X. Meng, K. Cheng, D.-Y. Xu, and C. Wu, Pure and Applied Chemistry, **78**, 1253, (2006).

52 M. Alaya, C. Chazelas, A. Vardelle, Journal of Therm Spray Technollogy **25**(1/2), 36, (2016).

53 P. Liang, J. P. Trelles, Plasma Sources Science and Technology **28**, 115012 (2019).

54 O. Colomés, S. Badiac, R. Codina, J.Principe, Comput. Methods Appl. Mech. Engrg. 285 (2015) 32–63.

55 J. Principe, R. Codina, F. Henke. Comput. Methods Appl. Mech. Engrg. 199 (13) (2010) 791–801

56 O. Guasch, R. Codina. Comput. Methods Appl. Mech. Engrg. 261–262 (2013) 154–166.